Materials Science & Engineering A 739 (2019) 53–61

Contents lists available at ScienceDirect

Materials Science & Engineering A

journal homepage: www.elsevier.com/locate/msea

Synchronous improvement in strength and ductility of biomedical Co–Cr–Mo alloys by unique low-temperature heat treatment

Kosuke Ueki[a,*], Mai Abe[b], Kyosuke Ueda[a], Masaaki Nakai[c], Takayoshi Nakano[d], Takayuki Narushima[a]

[a] Department of Materials Processing, Tohoku University, 6-6-02, Aza-Aoba, Aramaki, Aoba-ku, Sendai 980-8579, Japan
[b] Institute of Multidisciplinary Research for Advanced Materials, Tohoku University, 2-1-1, Katahira, Aoba-ku, Sendai 980-8577, Japan
[c] Department of Mechanical Engineering, Kindai University, 3-4-1, Kowakae, Higashiosaka 577-8502, Japan
[d] Division of Materials and Manufacturing Science, Osaka University, 2-1, Yamada-Oka, Suita, Osaka 565-0871, Japan

ARTICLE INFO

Keywords:
Heat treatment
Mechanical properties
Plastic deformation
Stacking fault
Strain-induced martensitic transformation

ABSTRACT

The microstructure and tensile properties of Co–27Cr–6Mo (mass%) alloys heat-treated at 673–1373 K were studied. Lower elongation was observed after heat treatment at 1073 K due to formation of carbonitride precipitates. In contrast, when low-temperature heat treatment (LTHT) was applied at 673–873 K, both the ultimate tensile strength and elongation synchronously improved compared with the solution-treated alloy. Electron backscatter diffraction analysis for plastic-strained alloys and in situ X-ray diffraction analysis under stress-induced conditions revealed that the strain-induced martensitic transformation (SIMT) of the γ(fcc)-phase to ε(hcp)-phase during plastic deformation was suppressed by the LTHT. Stacking faults (thin ε-phase) were observed to collide in the LTHT alloys. The following mechanisms for the synchronous improvement in the tensile strength and elongation after LHTH are proposed. First, stacking faults with multiple variants were formed during LTHT. Then, the ε-phase of a single variant formed by SIMT during plastic deformation collides with preexisting multi-variant stacking faults formed during LTHT, increasing the tensile strength. In addition, the SIMT during plastic deformation is suppressed in the high-plastic-strain region by the collision. This decreases the total amount of ε-phase formed during plastic deformation, which improves the ductility. We demonstrated that LTHT of Co–Cr–Mo alloys effectively improves the performance and mechanical safety of spinal fixation implants, which often fracture because of fatigue cracking.

1. Introduction

ASTM F75 Co–28Cr–6Mo (CCM; mass%) alloys are widely used in medical devices such as the sliding parts of artificial joints and spinal fixation implants because of their excellent strength, corrosion resistance, and wear resistance [1–3]. However, CCM alloys have poor ductility and workability because their stacking fault energy (SFE) is low and the γ (fcc)-phase to ε (hcp)-phase martensitic transformation easily occurs during plastic deformation [4,5]. Thus, the ductility and workability of CCM alloys needs to be improved in order to increase the safety and lifetime of medical implants.

The relationship between the microstructure and mechanical properties of CCM alloys has been investigated from the viewpoint of thermomechanical treatments, such as grain refinement by dynamic recrystallization and formation of the ε-phase from the γ-phase by strain-induced martensitic transformation (SIMT) [4–11]. Our previous studies showed that the ASTM F90 Co–20Cr–15W–10Ni (CCWN; mass %) alloy showed increased ductility, while maintaining high strength, after low-temperature heat treatment (LTHT) at 673 and 873 K [12,13]. The ε-phase formation as a result of SIMT was suppressed in the early-to-middle stages (plastic strain $< 35\%$) of plastic deformation for the LTHT alloys. In addition, the ε-phase formation at the grain boundaries was suppressed in the high-strain region (plastic strain $> 50\%$) of the LTHT alloy, and the stacking fault density increased. Based on these results, it was concluded that the stacking faults formed by LTHT inhibited SIMT for strains $\leq 50\%$. Consequently, the formation of the ε-phase at grain boundaries in the high-strain region ($> 50\%$) is suppressed, and stress concentrations at grain boundaries decrease. This suppressed crack generation and the subsequent propagation at the grain boundary and improves the mechanical properties. The CCM alloy

* Corresponding author at: Department of Materials Processing, Tohoku University, 6-6-02, Aza-Aoba, Aramaki, Aoba-ku, Sendai 980-8579, Japan.
E-mail addresses: kosuke.ueki.p8@dc.tohoku.ac.jp (K. Ueki), mai.abe.q4@dc.tohoku.ac.jp (M. Abe), ueda@material.tohoku.ac.jp (K. Ueda), nakai@mech.kindai.ac.jp (M. Nakai), nakano@mat.eng.osaka-u.ac.jp (T. Nakano), narut@material.tohoku.ac.jp (T. Narushima).

https://doi.org/10.1016/j.msea.2018.10.016
Received 11 July 2018; Received in revised form 2 October 2018; Accepted 4 October 2018
Available online 10 October 2018

Table 1
Chemical composition of the alloy used in this study (mass%).

Co	Cr	Mo	Si	Mn	N	C
Bal.	27.47	6.41	0.77	0.64	0.17	0.06

has a lower SFE at room temperature than the CCWN alloy, and the SIMT is known to occur preferentially during plastic deformation [6–9,14]. LTHT of this low-SFE alloy has not yet been reported. Therefore, this study investigated the influence of heat treatment on the tensile properties of the biomedical CCM alloy with a focus on the microstructural changes during heat treatment and plastic deformation.

2. Experimental

2.1. Materials

A forged CCM alloy bar with a diameter (ϕ) of 36 mm and chemical composition as listed in Table 1 was used as the base alloy. This as-received alloy bar was cut into cylinders with dimensions of ϕ = 6 mm × 40 mm. The cylindrical alloy specimens were then sealed inside SiO_2 ampoules in an Ar atmosphere at a pressure of approximately 0.02–0.03 MPa and temperature of 298 K (25 °C) to avoid their decarburization and/or denitrization during heat treatment [15,16]. As carbonitride precipitates were observed in the as-received alloy [17], solution treatment (ST) was conducted at 1523 K for 1.8 ks before heat treatment. The heat treatment was performed for up to 259.2 ks at 673–1373 K. Fig. 1 shows scanning electron microscopy-backscattered electron (SEM-BSE) images of the as-received and ST alloys. Precipitates were completely dissolved through ST at 1523 K.

2.2. Tensile testing

Tensile tests were conducted using a mechanical testing machine (RTF-1325, A&D Company Ltd., Tokyo, Japan). The ST and LTHT alloy bars were machined into samples with a gauge length of 10 mm and ϕ = 3 mm and then tested at a nominal strain rate of $1.67 \times 10^{-4}\ s^{-1}$ at room temperature (293 K). The elongation is defined as the rate of change of the gauge length before deformation relative to the gauge length at the fractured point. The test was conducted three times for each heat-treatment condition, and the average values of ultimate tensile strength, 0.2% proof strength, and elongation were calculated.

2.3. Microstructural observation

The microstructure of the heat-treated alloys was observed using SEM-BSE. The phase of the carbonitride precipitates detected in these alloys was identified using a combination of electrolytic extraction and X-ray diffraction (XRD). Electrolytic extraction was performed at 4 V for 10.8 ks in a $10H_2SO_4$–$90CH_3OH$ (vol%; equivalent to $20.5H_2SO_4$–$79.5CH_3OH$ mass%) solution. The precipitates electrolytically extracted from the alloys were collected as residue after filtering the electrolyte and analyzed by XRD [15–19]. The microstructures of the ST and LTHT alloys with induced plastic strains of 0%, 4%, 10%, and that required to fracture the sample were analyzed by electron backscatter diffraction (EBSD, JSM-7800F, JEOL Ltd., Tokyo,

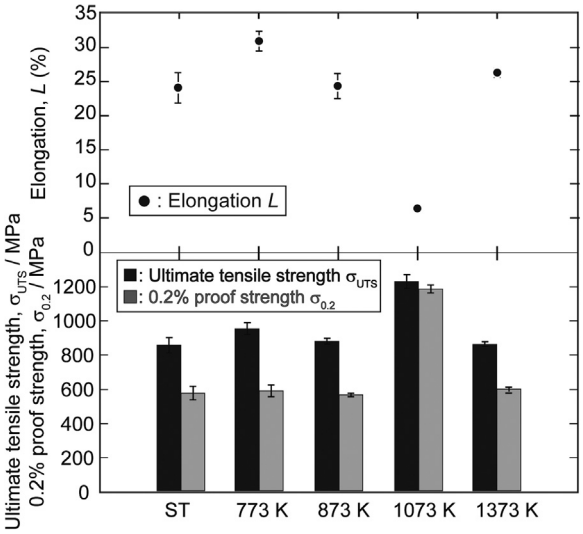

Fig. 2. Mechanical properties of the ST alloy and alloys heat treated at 673–1373 K for 259.2 ks.

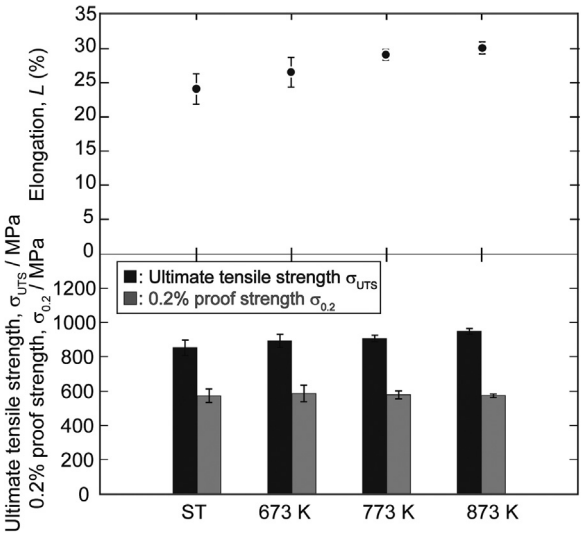

Fig. 3. Mechanical properties of the alloys heat treated at 673–873 K for 14.4 ks.

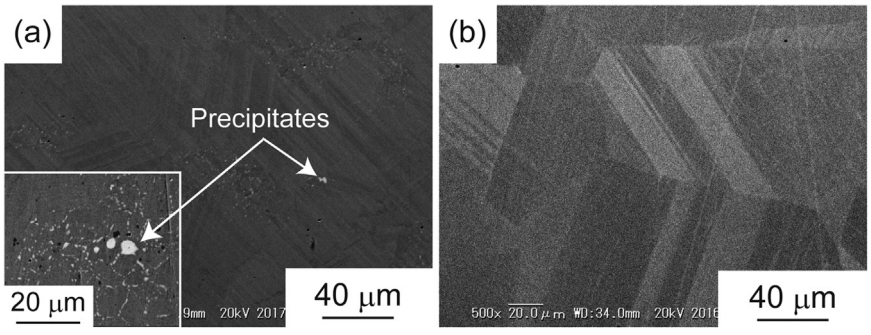

Fig. 1. SEM-BSE images of the (a) as-received and (b) ST alloys.

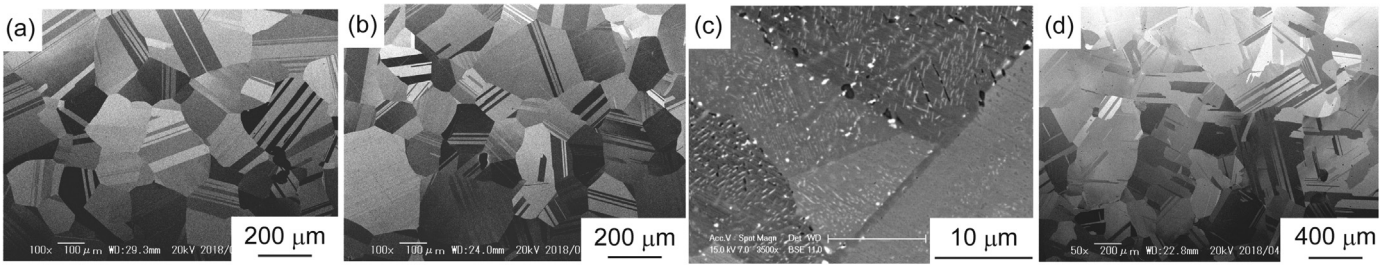

Fig. 4. SEM-BSE images of the (a) ST alloy and alloys heat treated at (b) 773 K, (c) 1073 K, and (d) 1373 K for 259.2 ks.

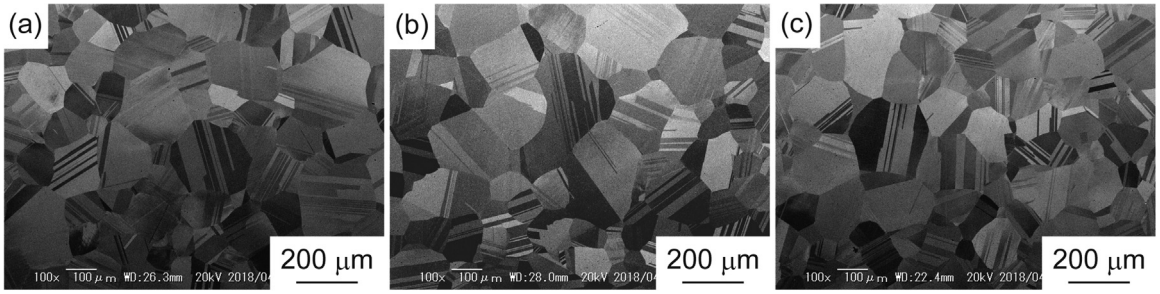

Fig. 5. SEM-BSE images of the alloys heat treated at (a) 673 K, (b) 773 K, and (c) 873 K for 14.4 ks.

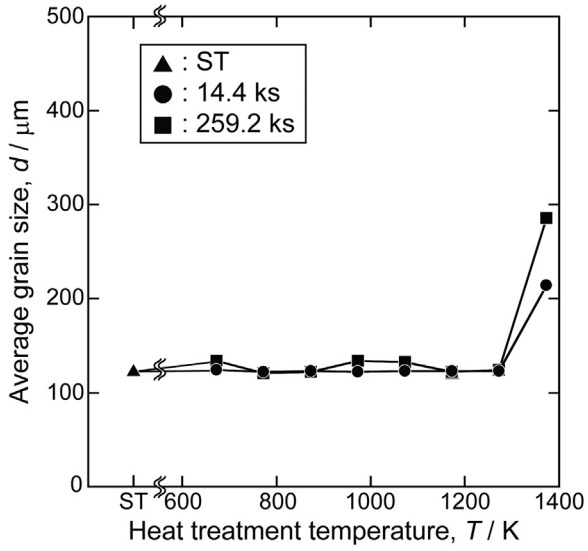

Fig. 6. Effect of heat treatment on the average grain size of the alloys.

Japan). A plastic strain of 0% means no plastic strain. The specimens with induced plastic strain were prepared for EBSD analysis by stopping tensile testing at plastic strain amplitudes of 4% and 10%. The surfaces of the specimens for EBSD observation were mechanically mirror polished and then vibration polished with colloidal silica [19]. The average value of the ε-phase fraction was calculated from four EBSD phase maps per specimen.

Transmission electron microscopy (TEM, JEM-2100, JEOL Ltd., Tokyo, Japan) was conducted on the ST and LTHT alloys. First, the specimens for TEM analysis were thinned to approximately 100 μm in thickness by mechanical polishing. Then, jet polishing was performed in a $10H_2SO_4$–$90CH_3OH$ (vol%; equivalent to $20.5H_2SO_4$–$79.5CH_3OH$ mass%) solution to remove any surface damage introduced during mechanical polishing that could influence the microstructural analysis. The jet-polished specimens were further thinned by ion milling (PIPS, Model 691, GATAN, Inc.) before TEM analysis.

2.4. In situ XRD analysis

In order to analyze the deformation structure, the phases of the metallic matrix were identified with in situ XRD (D8 Discover, Bruker AXS K.K., Karlsruhe, Germany) while the stress was varied. XRD specimens were machined to achieve a gauge length of 13 mm and rectangular cross-section of 3.5 × 0.7 mm. This was followed by LTHT at 773 K for 259.2 ks inside the SiO_2 ampoules. After a thin oxide surface film was removed via mechanical polishing, the alloy specimens were electrolytically mirror polished to eliminate the surface damage induced by machining. Electrolytic polishing was performed at a DC voltage difference of 6 V at 273 K (0 °C) for 30 s in a $10H_2SO_4$–$90CH_3OH$ (vol%; equivalent to $20.5H_2SO_4$–$79.5CH_3OH$ mass %) solution. In situ XRD analysis was conducted over the 2θ range of 20–80° using Cu Kα radiation and a two-dimensional X-ray detector under applied stress conditions. In order to maintain the intensity of the diffracted X-rays, the detection time was increased in the high 2θ angle region. The amount of total strain was calculated by measuring the specimen gauge length. In order to obtain diffracted X-rays from many grains, the XRD measurements were performed while the specimen was being swung.

3. Results

3.1. Tensile properties

Fig. 2 shows the tensile test results for the ST alloy and the alloy heat-treated at 773–1373 K for 259.2 ks. The ultimate tensile strength, 0.2% proof strength, and elongation of the ST alloy were 856 MPa, 575 MPa, and 24%, respectively. The ductility of the alloy heat treated at 1073 K was less than 10%, while the strength was higher than that of the ST alloy. The tensile strength and elongation of the alloy heat treated at 1373 K were almost the same as those of the ST alloy. For the LTHT alloys (773 and 873 K), both the tensile strength and elongation were higher than those of the ST alloy. The effect of the heat treatment time on the tensile properties was investigated with a focus on LTHT at 673–873 K. Fig. 3 shows the tensile test results of the alloys heat treated at 673–873 K for 14.4 ks. The tensile strength and elongation increased with the heat treatment temperature from 673 to 873 K. In the alloys heat treated at 773 K, the tensile strength and elongation increased with

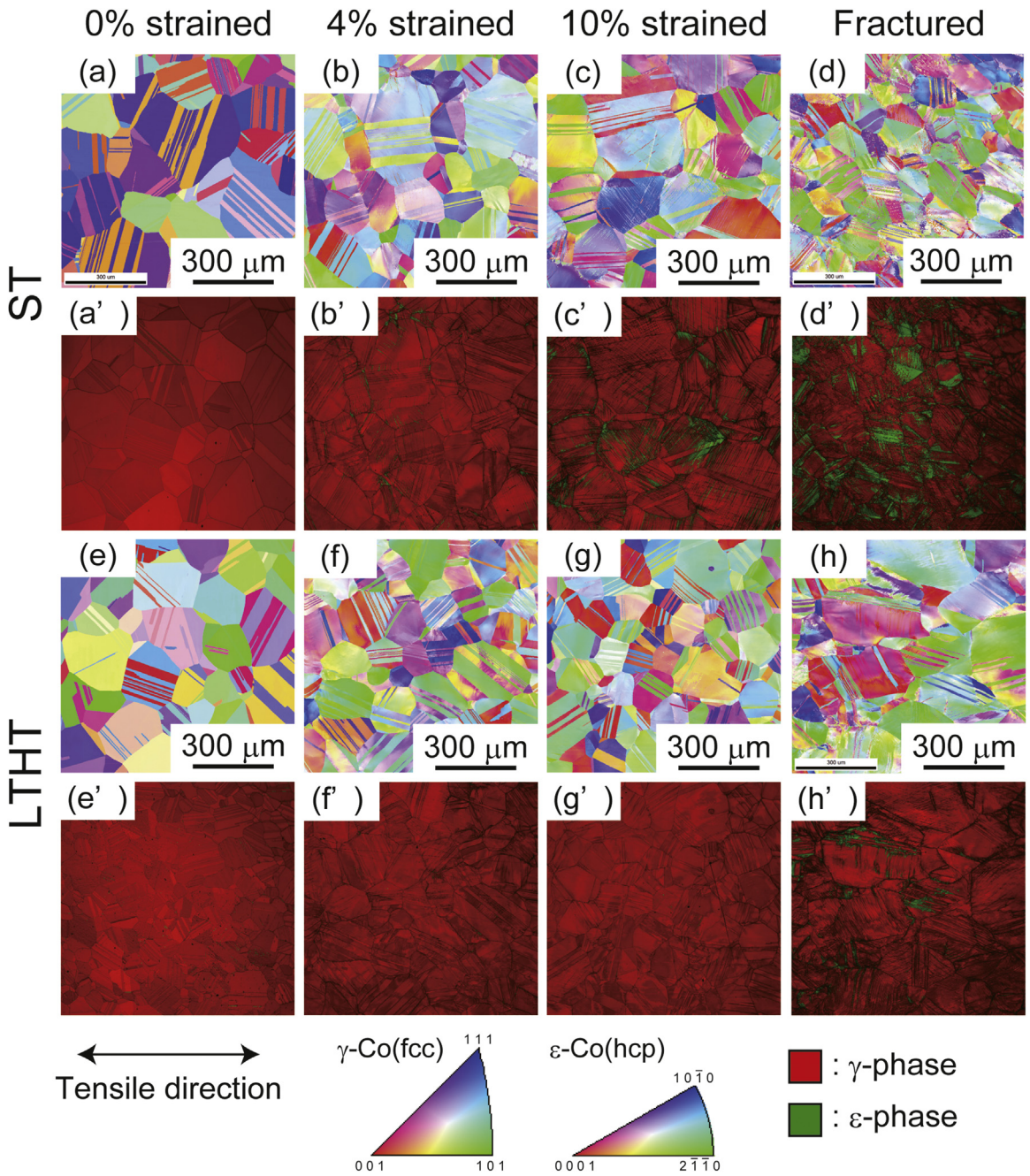

Fig. 7. (a–h) Low-magnification EBSD IPF and (a′–h′) phase maps of the (a, a′) 0% strain, (b, b′) 4% strain, (c, c′) 10% strain, and (d, d′) fractured specimens of the ST alloy and the (e, e′) 0% strain, (f, f′) 4% strain, (g, g′) 10% strain, and (h, h′) fractured specimens of the LTHT (773 K, 259.2 ks) alloy.

the heat treatment time. However, the alloys heat treated at 873 K for 14.4 ks showed higher tensile strength and elongation than those treated for 259.2 ks. Regardless of the heat-treatment time, all LTHT alloys showed higher tensile strength and elongation compared with the ST alloy. In particular, the alloy heat treated at 773 K for 259.2 ks showed the highest 0.2% proof strength, ultimate tensile strength, and elongation among the LTHT alloys, with values of 588 MPa, 953 MPa, and 31%, respectively.

3.2. Microstructure

Fig. 4 shows SEM-BSE images of the ST alloy and alloys heat treated at 773–1373 K for 259.2 ks. In the case of the alloy heat treated at 1073 K, three types of precipitates were observed. Specifically, white, gray, and black carbonitride precipitates formed at 1073 K after ST, attributed to the η-phase (M_6X-$M_{12}X$ type), π-phase (M_2T_3X type), and $M_{23}X_6$ type (M and T: metallic elements, X: C and/or N), respectively [15–20]. The area fraction of these precipitates was 10.2%. Hence, we attributed the increase in tensile strength and decrease in ductility of the alloy heat treated at 1073 K to the formation of these precipitates. No precipitates were observed in the alloys heat treated at 773 and 1373 K, even for 259.2 ks. Fig. 5 shows SEM-BSE images of the alloys subjected to LTHT for 14.4 ks. No carbonitride precipitates were detected in the LTHT alloy at 873 K.

The average grain sizes of the alloys were calculated from these SEM-BSE images, as shown in Fig. 6. The average grain size of the ST alloy was 124 μm. In the alloys heat treated up to 1073 K, the average grain size was 120–130 μm, which was not significantly different to that of the ST alloy. Hence, no microstructural changes at the level observable by SEM occurred in the LTHT alloys compared to the as-

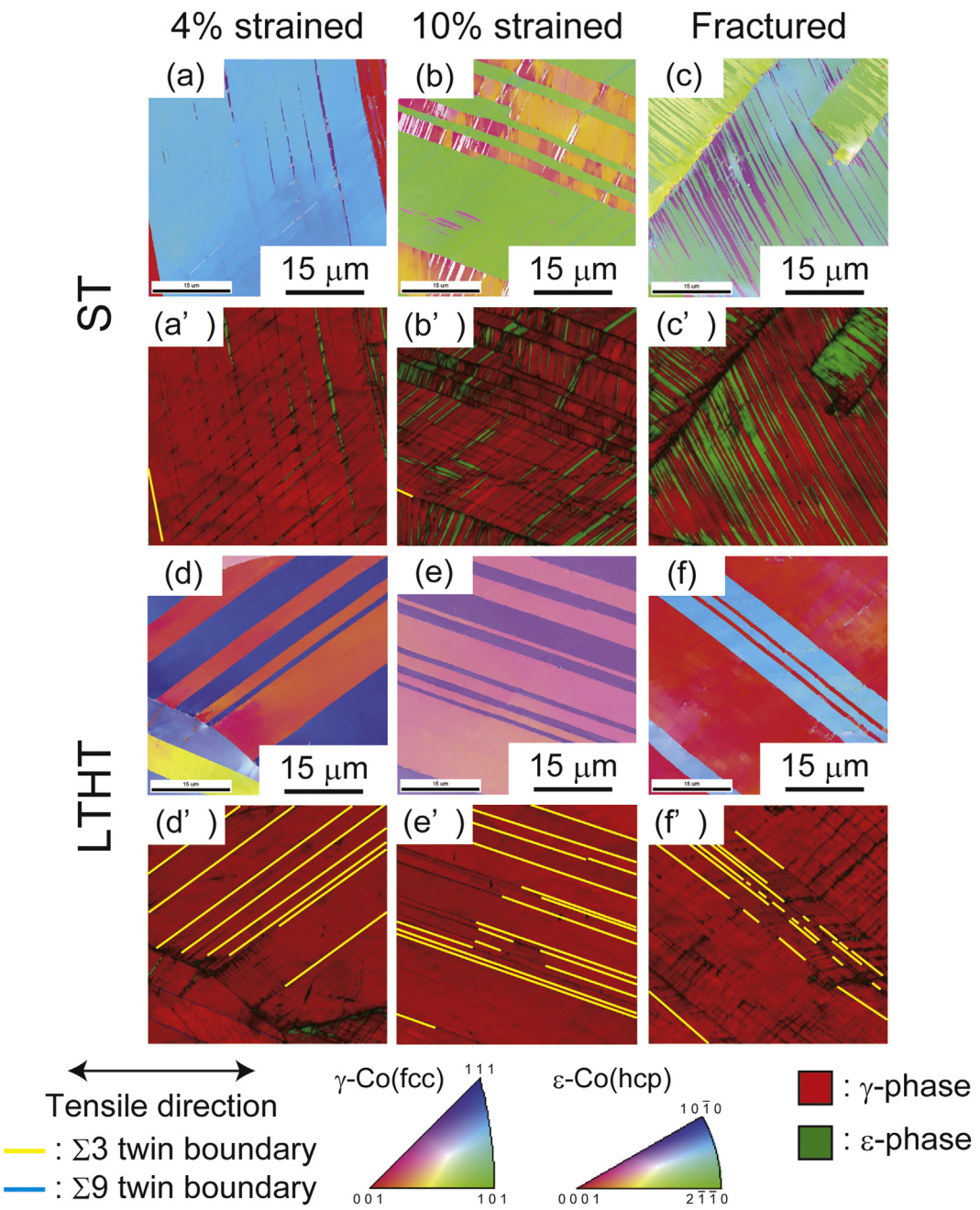

Fig. 8. High-magnification (a–f) EBSD IPF and (a′–f′) phase maps of the (a, a′) 4% strain, (b, b′) 10% strain, and (c, c′) fractured specimens of the ST alloy and the (d, d′) 4% strain, (e, e′) 10% strain, and (f, f′) fractured specimens of the LTHT (773 K, 259.2 ks) alloy.

received alloy.

3.3. Microstructure after plastic deformation

Fig. 7 shows the EBSD inverse pole figure (IPF) and phase maps of the ST alloy and alloy heat treated at 773 K for 259.2 ks (LTHT alloy) after the introduction of plastic strains of 0%, 4%, and 10%, and that at the fracture point. The highest strength and elongation were detected under the LTHT conditions. The plastic strains at the fracture points were 24% and 31% for the ST and LTHT alloys, respectively. All of the 0% and 4% plastic strain alloys mostly contained a single γ-phase. In the 10% plastic strain samples, the ε-phase formed by SIMT was observed in the ST alloy, while the matrix in the LTHT alloy was mostly single γ-phase. For the fractured specimens, although the ε-phase formed by SIMT was observed in both ST and LTHT alloys, the former had a much larger amount. In order to clarify the morphology and distribution of strain-induced ε-phase, high-magnification EBSD analysis of the strained alloys was conducted, as shown in Fig. 8. In the case of the ST alloys, a large amount of band-like ε-phase formed by SIMT was observed, while only a very small amount of ε-phase was observed in the strained LTHT alloys. In addition, in the strained ST alloys, some ε-phase occurred at twin boundaries. These results were in good agreement with the images shown in Fig. 7. Fig. 9 shows the ε-phase fraction (f_ε) calculated from the EBSD phase maps in Fig. 7 at each plastic strain. These results clearly show that there was no significant difference in f_ε between the ST and LTHT alloys in the low-strain region (plastic strain ≤ 4%). However, in the high-strain region, the formation of the ε-phase by SIMT was suppressed by the LTHT. The LTHT alloy had a lower f_ε than the ST alloy at the fracture point, although it had more plastic strain.

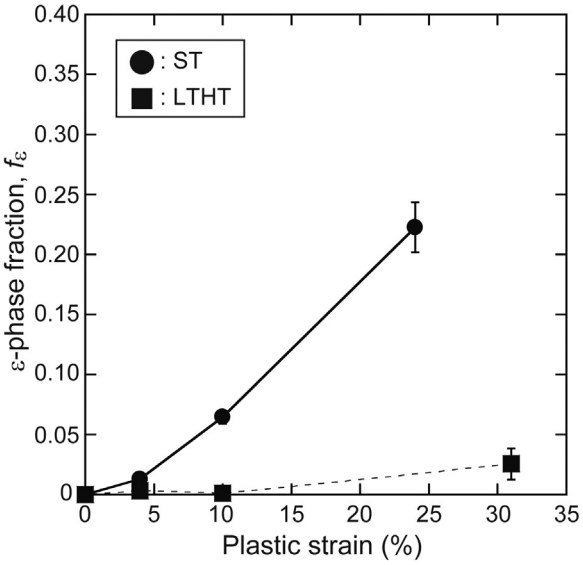

Fig. 9. Effect of plastic deformation on the ε-phase fraction of the ST and LTHT (773 K, 259.2 ks) alloys calculated from low-magnification EBSD phase maps.

4. Discussion

4.1. Strain-induced martensitic transformation during plastic deformation

The results of the EBSD analysis shown in Figs. 7–9 clearly indicated that the change in SIMT behavior during plastic deformation contributed to the improvement of the tensile properties with LTHT. Therefore, in situ XRD was performed on the ST and LTHT alloys under applied stress, where the results are shown in Fig. 10.

The plastic strains at the fracture points of the ST and LTHT alloys were 33% and 53%, respectively, which confirmed that LTHT increased the ductility. Based on the XRD peak intensities, f_ε was calculated as follows [21]:

$$f_\gamma = I_{\gamma\{200\}}/(I_{\gamma\{200\}} + 1.5I_{\varepsilon\{10-10\}}) \quad (1)$$

$$f_\varepsilon = 1-f_\gamma \quad (2)$$

where, $I_{\gamma\{200\}}$ and $I_\varepsilon\{10\bar{1}0\}$ are the peak intensities for {200} of the γ-phase and {10−10} of the ε-phase, respectively, and f_γ is the γ-phase fraction. Fig. 11 shows the values of f_ε determined for the ST and LTHT alloys. For both alloys, f_ε increased in the early stages of plastic deformation, although the increase in f_ε was small for the LTHT alloy compared with that for the ST alloy. After the fast increase, f_ε increased linearly with increasing total strain. The sharp increase in f_ε at the early stage of plastic deformation was suppressed by the LTHT.

The absolute values of f_ε calculated from the EBSD phase maps and from the in situ XRD analysis differed due to differences in the sample shapes and analysis region. Similar to our previous study, the specimens

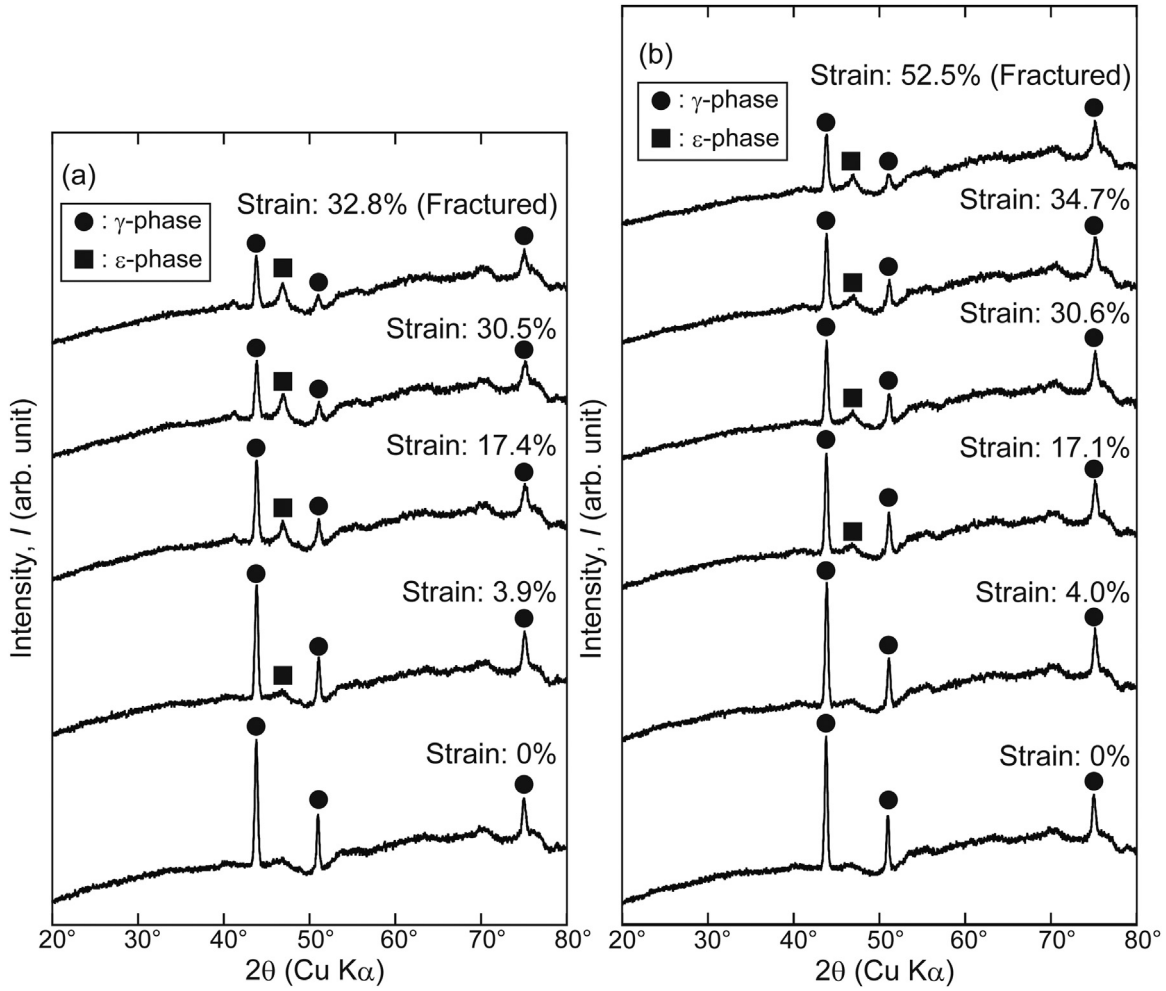

Fig. 10. *In situ* XRD patterns obtained for the (a) ST and (b) LTHT (773 K, 259.2 ks) alloys.

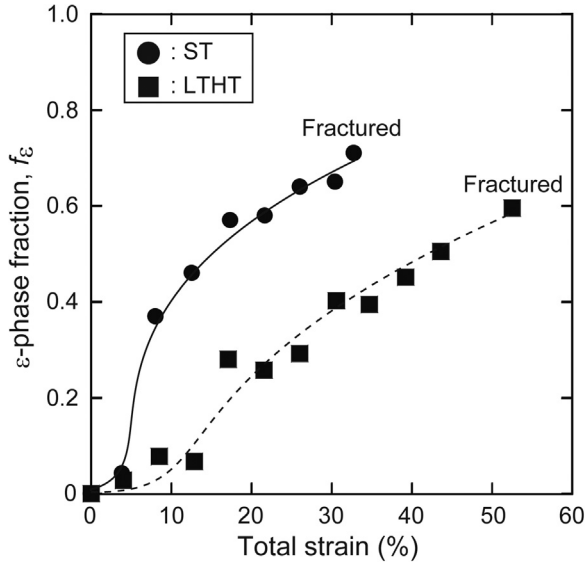

Fig. 11. ε-phase fraction (calculated from XRD peak intensity ratios) as a function of total strain during plastic deformation of the ST and LTHT (773 K, 259.2 ks) alloys.

for EBSD analysis were made from a rod-shaped alloy that was halved in the longitudinal direction [13]; the center of these specimens was analyzed. In contrast, the in situ XRD analysis was performed on plate-like specimens, and the microstructure of the specimen surface was analyzed. Although these factors resulted in different f_ε values, both methods indicated that the LTHT alloy had a lower f_ε than the ST alloy after plastic deformation.

4.2. Mechanism for improved mechanical properties after LTHT

The LTHT increased both the ductility and tensile strength, as shown in Figs. 2 and 3. This phenomenon cannot be explained merely by the suppression of ε-phase formation. Sorensen et al. reported that the strength of the Co–35Ni–20Cr–10Mo (MP35N) alloy was improved by segregating Mo into stacking faults [22]. In order to investigate this possibility, elemental line analysis was performed on the LTHT alloys using bright-field (BF) TEM combined with energy dispersive X-ray spectroscopy (EDS). These results are shown in Fig. 12, where no segregation of Mo in the stacking faults was observed. Sorensen et al. reported segregation in a MP35N alloy that was heat-treated at 973 K for 60 s after 36–60% cold working [22]. In the present study, the heat-treatment temperature was 100–300 K lower than that reported in this previous study. Thus, we concluded that segregation of Mo in stacking faults did not occur to a significant degree under the heat treatment conditions used in this study. Hence, the improved tensile strength by LTHT was not due to Mo segregation.

TEM was used for microstructural analysis on **B** // [111] for the ST alloy and LTHT (773 K, 259.2 ks) alloys with 0% and 10% plastic strains. The results are shown in Fig. 13. Without deformation (0% plastic strain), stacking faults with multiple variants were observed in the LTHT alloy (Fig. 13(a)), while stacking faults with a single variant were observed in the ST alloy (Fig. 13(c)). Weak diffraction spots of the ε-phase were observed in both the ST and LTHT alloy (Fig. 13(a′), (c′)). The same tendency was confirmed in the alloys with 10% plastic strain (Fig. 13(b), (d)), where a large amount of stacking faults with a single variant was observed for the ST alloy. In the LTHT alloy, stacking faults with various variants were observed, and they collided or intersected. Clear diffraction spots of ε-phase were observed from both ST and LTHT alloys under 10% strain; a large amount of stacking faults (thin ε-phase) were formed by SIMT. Olson and Cohen defined the SFE of an alloy with the γ–ε martensitic transformation as follows [23]:

$$SFE = 2\rho\Delta G^{\gamma\rightarrow\varepsilon} + 2\rho^{\gamma/\varepsilon} \quad (3)$$

where, $\Delta G^{\gamma\rightarrow\varepsilon}$ is the Gibbs free energy change from the γ phase to ε phase, ρ is the atomic density of {111} in the γ-phase (3.06×10^{-5} m^{-2}), and $2\sigma^{\gamma/\varepsilon}$ is the γ–ε interfacial energy, which was 15 mJ m^{-2} in this study [24]. Eq. (3) was used to calculate the SFE of the alloys used in this study at 200–1600 K with the Thermo-Calc database TCFE 7. The results are shown in Fig. 14.

The CCM alloy has been reported to have a negative SFE at room temperature [6–9]. The alloy used in this study also had a negative SFE at room temperature (300 K). The SFE was also negative at the LTHT temperatures (673–873 K), although it was higher than the room-temperature value. Because the SFE was negative at 673–873 K, multiple variants of stacking faults (i.e., a thin ε-phase) might have formed. In other words, in addition to the stacking faults formed when the ST alloy was quenched, multiple variants of stacking faults formed during LTHT.

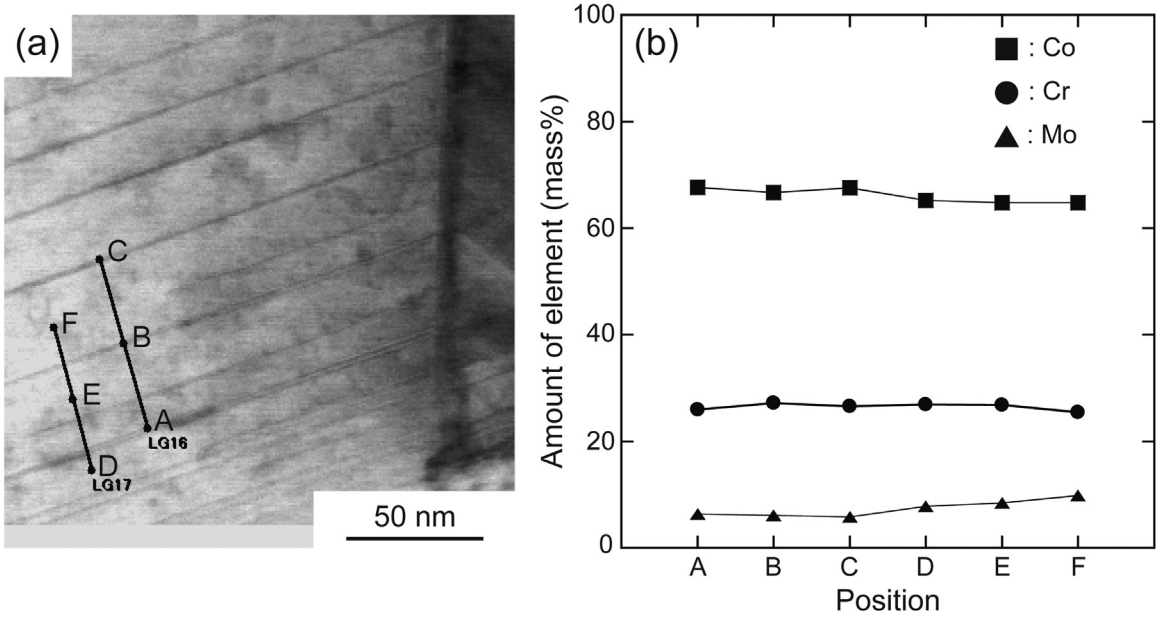

Fig. 12. (a) TEM-BF image and (b) results of the EDS analysis of the LTHT (773 K, 259.2 ks) alloy.

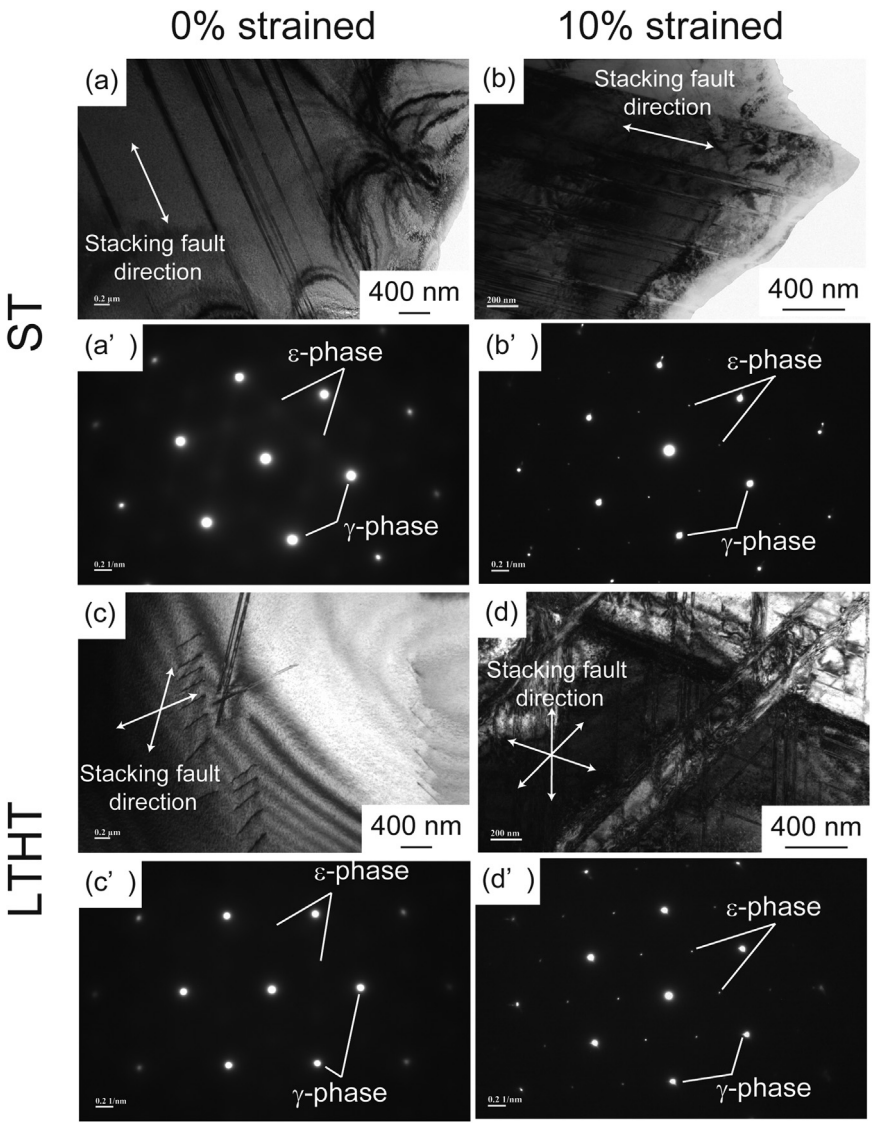

Fig. 13. (a–d) TEM-BF images and (a′–d′) selected area diffraction (SAD) patterns of the (a, a′, b, b′) ST alloy and (c, c′, d, d′) LTHT (773 K, 259.2 ks) alloy with (a, a′, c, c′) 0% and (b, b′, d, d′) 10% plastic strain.

Hence, collision or intersection with the ε-phase formed by SIMT occurred (see Fig. 12(b), (d)). Hagihara et al. reported that preexisting (111) ε-phase in a single crystal of the CCM alloy acted as a strong obstacle for the ε-phase formed during SIMT, which is not parallel to the preexisting ε-phase [17]. As shown in Figs. 8 and 10, the formation of the ε-phase by SIMT was suppressed by LTHT. The critical resolved shear stress (CRSS) when the strain-induced ε-phase intersects other ε-phases was reported to be ~ 125 MPa, which is much higher than that for the formation of a strain-induced ε-phase parallel to the preexisting ε-phase (54 MPa) [11]. In other words, it is extremely difficult for multiple variants of stacking faults formed by LTHT to intersect with the ε-phase single variant formed by SIMT. Therefore, the stacking faults (thin ε-phase) formed by LTHT inhibit the progress of SIMT, and the LTHT alloy demonstrate less ε-phase during plastic deformation compared to that of the ST alloy.

Based on these results, the tensile strength was improved by the collision between the stacking faults formed by LTHT and the ε-phase formed by SIMT. This improves the ductility as the ε-phase formed by LTHT inhibits the progress of SIMT during deformation. According to our finding, applying LTHT to the manufacturing process of spinal fixation implants made of CCM alloys should improve their workability and quality.

5. Conclusions

The microstructure and tensile properties of biomedical CCM alloys subjected to LTHT were investigated. Both the tensile strength and ductility were improved by LTHT at 673–873 K, while the LTHT alloys formed less ε-phase during plastic deformation than the ST alloy. LTHT formed multiple variants of stacking faults, which inhibited the progress of SIMT during plastic deformation, resulting in improved ductility. The tensile strength was improved by the collision between stacking faults formed by LTHT and the ε-phase formed by SIMT.

Acknowledgments

This study was financially supported by the Japan Society for the Promotion of Science KAKENHI [grant numbers JP 16J04279, 18H1718].

Data availability

The raw/processed data required to reproduce these findings cannot be shared at this time as the data also forms part of an ongoing study.

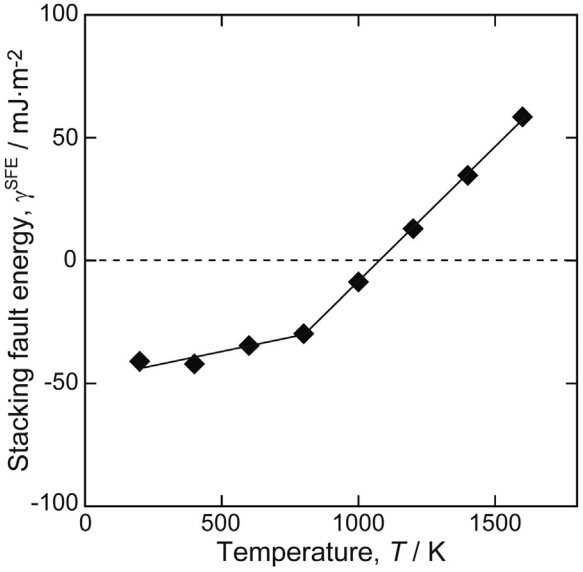

Fig. 14. Temperature dependence of the SFE of the CCM alloy used in this study.

References

[1] T.M. Devine, J. Wulff, Cast vs. wrought cobalt-chromium surgical implant alloys, J. Biomed. Mater. Res. 9 (1975) 151–167.

[2] M. Niinomi, T. Hanawa, T. Narushima, Japanese research and development on metallic biomedical, dental, and healthcare materials, JOM 57 (2005) 18–24.

[3] T. Narushima, K. Ueda, Alfirano, Co-Cr Alloys as Effective Metallic Biomaterials, in: M. Niinomi, T. Narushima, M. Nakai (Eds.), Advances in Metallic Biomaterials. Springer Series in Biomaterials Science and Engineering, 3 Springer, Berlin, Heidelberg, 2015, pp. 157–178.

[4] A. Chiba, S.H. Lee, H. Matsumoto, M. Nakamura, Construction of processing map for biomedical Co–28Cr–6Mo–0.16N alloy by studying its hot deformation behavior using compression tests, Mater. Sci. Eng. A 513–514 (2009) 286–293.

[5] M. Mori, K. Yamanaka, H. Matsumoto, A. Chiba, Evolution of cold-rolled microstructures of biomedical Co-Cr-Mo alloys with and without N doping, Mater. Sci. Eng. A 528 (2010) 614–621.

[6] Y. Koizumi, S. Suzuki, K. Yamanaka, B.-S. Lee, K. Sato, Y. Li, S. Kurosu, H. Matsumoto, A. Chiba, Strain-induced martensitic transformation near twin boundaries in a biomedical Co–Cr–Mo alloy with negative stacking fault energy, Acta Mater. 61 (2013) 1648–1661.

[7] K. Yamanaka, M. Mori, S. Kurosu, H. Matsumoto, A. Chiba, Ultrafine grain refinement of biomedical Co-29Cr-6Mo alloy during conventional hot-compression deformation, Metall. Mater. Trans. A 40 (2009) 1980–1994.

[8] K. Yamanaka, M. Mori, A. Chiba, Origin of significant grain refinement in Co-Cr-Mo alloys without severe plastic deformation, Metall. Mater. Trans. A 43 (2012) 4875–4887.

[9] K. Yamanaka, M. Mori, A. Chiba, Nanoarchitectured Co–Cr–Mo orthopedic implant alloys: nitrogen-enhanced nanostructural evolution and its effect on phase stability, Acta Biomater. 9 (2013) 6259–6267.

[10] S. Kurosu, H. Matsumoto, A. Chiba, C. Landron, D. Fabregue, E. Maire, The damage process in a biomedical Co–29Cr–6Mo–0.14N alloy analyzed by X-ray tomography and electron backscattered diffraction, Scr. Mater. 64 (2011) 367–370.

[11] K. Hagihara, T. Nakano, K. Sasaki, Anomalous strengthening behavior of Co–Cr–Mo alloy single crystals for biomedical applications, Scr. Mater. 123 (2016) 149–153.

[12] K. Ueki, K. Ueda, T. Narushima, Microstructure and mechanical properties of heat-treated Co-20Cr-15W-10Ni alloy for biomedical application, Metall. Mater. Trans. A 47 (2016) 2773–2782.

[13] K. Ueki, K. Ueda, M. Nakai, T. Nakano, T. Narushima, Microstructural changes during plastic deformation and corrosion properties of biomedical Co-20Cr-15W-10Ni alloy heat-treated at 873 K, Metall. Mater. Trans. A 49 (2018) 2393–2404.

[14] L. Rémy, A. Pineau, Twinning and strain-induced f.c.c. → h.c.p. transformation on the mechanical properties of Co-Ni-Cr-Mo alloys, Mater. Sci. Eng. 26 (1976) 123–132.

[15] S. Mineta, Alfirano, S. Namba, T. Yoneda, K. Ueda, T. Narushima, Precipitates in biomedical Co-28Cr-6Mo-(0–0.41) C alloys heat-treated at 1473 K to 1623 K (1200 °C to 1350 °C), Metall. Mater. Trans. A 43 (2012) 3351–3358.

[16] S. Mineta, S. Namba, T. Yoneda, T. Ueda, T. Narushima, Carbide formation and dissolution in biomedical Co-Cr-Mo alloys with different carbon contents during solution treatment, Metall. Mater. Trans. A 41 (2010) 2129–2138.

[17] K. Ueki, Y. Kurihara, S. Mineta, Alfirano, K. Ueda, S. Namba, T. Yoneda, T. Narushima, Changes in microstructure of biomedical Co-Cr-Mo alloys during aging at 973 to 1373 K, Mater. Trans. 57 (2016) 2048–2053.

[18] T. Narushima, S. Mineta, Y. Kurihara, K. Ueda, Precipitates in biomedical Co-Cr alloys, JOM 65 (2013) 489–504.

[19] H.S. Dobbs, J.L.M. Robertson, Heat treatment of cast Co-Cr-Mo for orthopaedic implant use, J. Mater. Sci. 18 (1983) 391–401.

[20] M. Gómez, H. Mancha, A. Salinas, J.L. Rodríguez, J. Escobedo, M. Castro, M. Méndez, Relationship between microstructure and ductility of investment cast ASTM F-75 implant alloy, J. Biomed. Mater. Res. 34 (1997) 157–163.

[21] M. Sage, C. Guillaud, Méthode d'analyse quantitative des variétés allotropiques du cobalt par les rayons X, Rev. Metall. 47 (1950) 139–145.

[22] D. Sorensen, B.Q. Li, W.W. Gerberich, K.A. Mkhoyan, Investigation of secondary hardening in Co–35Ni–20Cr–10Mo alloy using analytical scanning transmission electron microscopy, Acta Mater. 63 (2014) 63–72.

[23] G.B. Olson, M. Cohen, A general mechanism of martensitic nucleation: Part I. General concepts and the FCC → HCP transformation, Metall. Trans. 7 (1976) 1897–1904.

[24] A.P. Miodownik, The calculation of stacking fault energies in Fe-Ni-Cr alloys, Calphad 2 (1978) 207–226.